Electronic Supplementary Information (ESI) for
A New Avenue to Relaxor-like Ferroelectric Behaviour
Found by Probing the Structure and Dynamics of $(NH_3NH_2)Mg(HCO_2)_3$

Authors:

Thomas J. Hitchings,[1] Helen M. Wickins,[2] George U. L. Peat,[2] Paul Hodgkinson,[2] Anant Kumar Srivastava,[1] Teng Lu,[3] Yun Liu,[3] Ross Piltz,[4] Franz Demmel,[5] Anthony E. Phillips,[6] and Paul Saines.[1]

[1] School of Chemistry and Forensic Science, Ingram Building, University of Kent, Canterbury, Kent, CT2 7NH, United Kingdom.

[2] Department of Chemistry, Durham University, DH1 3LE, Durham, United Kingdom.

[3] Research School of Chemistry, The Australian National University, Canberra, ACT 2600, Australia

[4] Australian Nuclear Science and Technology Organisation, Lucas Heights, NSW 2234, Australia.

[5] ISIS Facility, Rutherford Appleton Laboratory, Didcot, OX11 0QX, United Kingdom.

[6] School of Physics and Astronomy, Queen Mary University of London, London, E1 4NS, United Kingdom.

Neutron Crystallography

Table S1: Neutron crystallographic data for $(NH_3NH_2)Mg(HCO_2)_3$. The unit cell parameters are refined from X-ray crystal structures using LaueG.

Identification code	Xtal2_250K_wav_Fin	Xtal2_300K_wav	Xtal2_330K_wav	Xtal2_350K_wav_Dis	Xtal2_400K_wav_NDis
Empirical formula	$C_3H_8MgN_2O_6$	$C_3H_8MgN_2O_6$	$C_3H_8MgN_2O_6$	$C_3H_8MgN_2O_6$	$C_3H_8MgN_2O_6$
Formula weight	192.41	192.41	192.41	192.41	192.34
Temperature/K	249.999	299.999	329.999	349.999	400.001
Crystal system	orthorhombic	orthorhombic	orthorhombic	hexagonal	Hexagonal
Space group	$P2_12_12_1$	$P2_12_12_1$	$P2_12_12_1$	$P6_3$	$P6_3$
a/Å	7.46	7.46	7.52	7.87	7.87
b/Å	7.87	7.88	7.88	7.87	7.87
c/Å	13.69	13.67	13.66	7.56	7.56
$\alpha/°$	90	90	90	90	90
$\beta/°$	90	90	90	90	90
$\gamma/°$	90	90	90	120	120
Volume/Å^3	803.7	803.6	809.5	405.5	405.5
Z	4	4	4	2	2
ρ_{calc}/g/cm^3	1.590	1.590	1.579	1.576	1.576
μ/mm^{-1}	0.154	0.154	0.152	0.152	0.152
F(000)	196.0	196.0	196.0	98.0	98.0
Crystal size/mm	1.4 x 1.1 x 0.6	1.4 x 1.1 x 0.6	1.4 x 1.1 x 0.6	1.4 x 1.1 x 0.6	1.4 x 1.1 x 0.6
Radiation	neutrons ($0.85 \leq \lambda < 1.7$Å)	neutrons ($0.85 \leq \lambda < 1.7$Å)	neutrons ($0.85 \leq \lambda < 1.7$Å)	neutrons ($0.85 \leq \lambda < 1.7$Å)	neutrons ($0.85 \leq \lambda < 1.7$Å)
2Θ range for data collection/°	8.756 to 67.472	8.4 to 59.992	8.402 to 67.484	8.414 to 72.036	8.414 to 72.078
Index ranges	$-8 \leq h \leq 8, -8 \leq k \leq 8, -12 \leq l \leq 12$	$-7 \leq h \leq 7, -7 \leq k \leq 7, -13 \leq l \leq 13$	$-7 \leq h \leq 7, -8 \leq k \leq 8, -14 \leq l \leq 14$	$-8 \leq h \leq 8, -8 \leq k \leq 9, -8 \leq l \leq 8$	$-8 \leq h \leq 8, -8 \leq k \leq 9, -8 \leq l \leq 8$
Reflections collected	6555	4659	7269	4556	4285
Independent reflections	870 [R_{int} = 0.7820, R_{sigma} = 0.4417]	695 [Rint = 0.6109, Rsigma = 0.2955]	953 [R_{int} = 0.5301, R_{sigma} = 0.2633]	381 [R_{int} = 0.3380, R_{sigma} = 0.1344]	384 [R_{int} = 0.3349, R_{sigma} = 0.1384]
Data/restraints/parameters	870/73/114	695/134/120	953/136/120	381/33/75	384/57/72
Goodness-of-fit on F^2	1.046	1.117	1.070	1.078	1.154
Final R indexes [I>=2σ (I)]	R_1 = 0.1292, wR_2 = 0.2550	R_1 = 0.1389, wR_2 = 0.3161	R_1 = 0.1347, wR_2 = 0.2855	R_1 = 0.0668, wR_2 = 0.1274	R_1 = 0.0760, wR_2 = 0.1704
Final R indexes [all data]	R_1 = 0.2499, wR_2 = 0.2997	R_1 0.2730, wR_2 = 0.3948	R_1 = 0.2339, wR_2 = 0.3468	R_1 = 0.1029, wR_2 = 0.1373	R_1 = 0.1223, wR_2 = 0.1861
Largest diff. peak/hole / e Å^{-3}	1.07/-0.92	0.66/-0.77	0.81/-0.95	0.53/-0.45	0.58/-0.49

PLATON ADDSYYM detects pseudo symmetry and suggests the space group $P6_322$ for the high temperature phase. Upon solving the structure in this symmetry, it is difficult to obtain a good structural model, with the refinement statistics considerably poorer than expected and all non-metal atoms refining as a non-positive difference. The additional suggested symmetry would divide the reoriented cation in half resulting in two equivalent NH_3 groups, and is likely flagged by the dfix and SUMP restraints. From a chemical perspective, the additional symmetry would enforce an eclipsed conformation on the hydrogen atoms of the NH_3 groups, whilst the confirmation in the lower symmetry $P6_3$ is more staggered, which is usually more energetically favourable.

Table S2: The refined occupancy of the nitrogen positions using the atom labelling of Fig. 1. N4 and N5 are on 2a Wyckoff position and N3 is on the 6c general position in the high temperature phase with all N atoms on 4a general positions at low temperature.

Temperature / K	Nominal N Stoichiometry	N1	N2a	N2b	N3	N4	N5
250	2	1	0.89(4)	0.11(4)	-	-	-
300	2	1	0.58(6)	0.42(6)	-	-	-
330	2	1	0.62(3)	0.38(3)	-	-	-
350	2	-	-	-	0.44(4)	0.34(6)	0.34(6)
400	2	-	-	-	0.44(4)	0.35(7)	0.35(7)

Table S3: The occupancies of the H positions in the NH_3NH_2 cation, fixed to be approximately equal to the N they are bonded to in the low temperature phase and then refined using the SHELX SUMP command to fix the maximum occupancies across all H sites to 5 in the high temperature phase. H13 is on the 2a Wyckoff position, with H11 and H12 on 6c general positions in the high temperature phase, with all H atoms on 4a general positions at low temperature.

Temperature (K)	Nominal H Stoichiometry	H1 a, b, c Occupancy	H2 a Occupancy	H2 b Occupancy	H3 Occupancy	H11 Occupancy	H12 Occupancy	H13 Occupancy
250	5	1	0.88	0.12	1	-	-	-
300	5	1	0.58	0.42	1	-	-	-
330	5	1	0.62	0.38	1	-	-	-
350	5	-	-	-	-	0.66(10)	0.92(10)	0.38(5)
400	5	-	-	-	-	0.50(10)	1.05(9)	0.35(17)

Table S4: Values associated with the hydrogen bonding between the cation and the framework for the low temperature phase at 250 K.

X-H···Y	H···Y Å	X···Y Å	X-H···Y °
N2b-H2b···O6	2.2(2)	3.19(14)	138(17)
N2a-H2a···O5	2.52(6)	3.28(3)	120(4)
N2a-H3···O4	2.15(5)	3.31(3)	168(6)
N2b-H3···O4	2.15(5)	2.67(5)	102(4)
N2a-H3···O1	2.22(6)	2.83(3)	109(4)
N2b-H3···O1	2.22(6)	3.42(6)	176(9)
N1-H1b···N2a	2.08(6)	3.17(4)	153(5)
N1-H1a···O6	1.86(4)	3.00(3)	159(5)

Table S5: Values associated with the hydrogen bonding between the cation and the framework for the high temperature phase at 400 K.

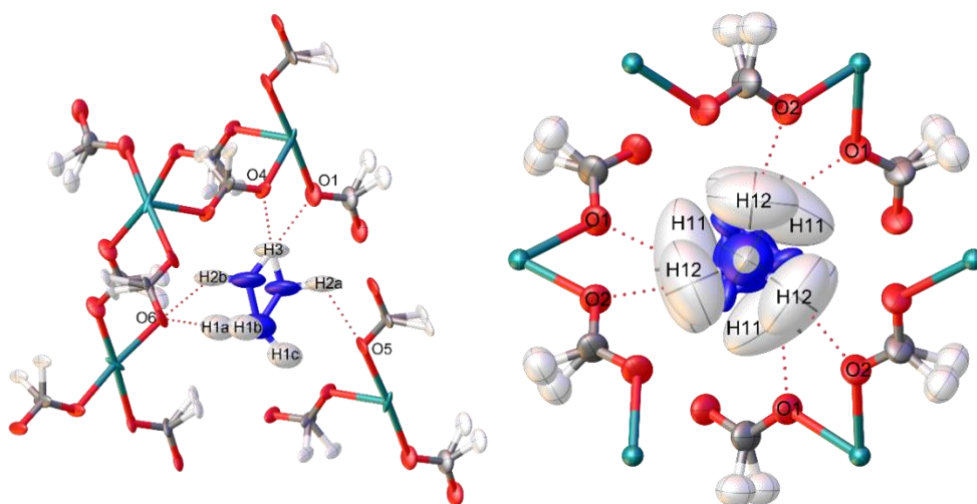| X-H⋯Y	H⋯Y Å	X⋯Y Å	X-H⋯Y °
N4-H11⋯O1	1.89(8)	3.142(12)	171(10)
N5-H12⋯O2	2.26(10)	3.159(14)	126(5)

Fig. S1: The hydrogen bonding between the cation and the framework at (*left*) 250 K and (*right*) 400 K.
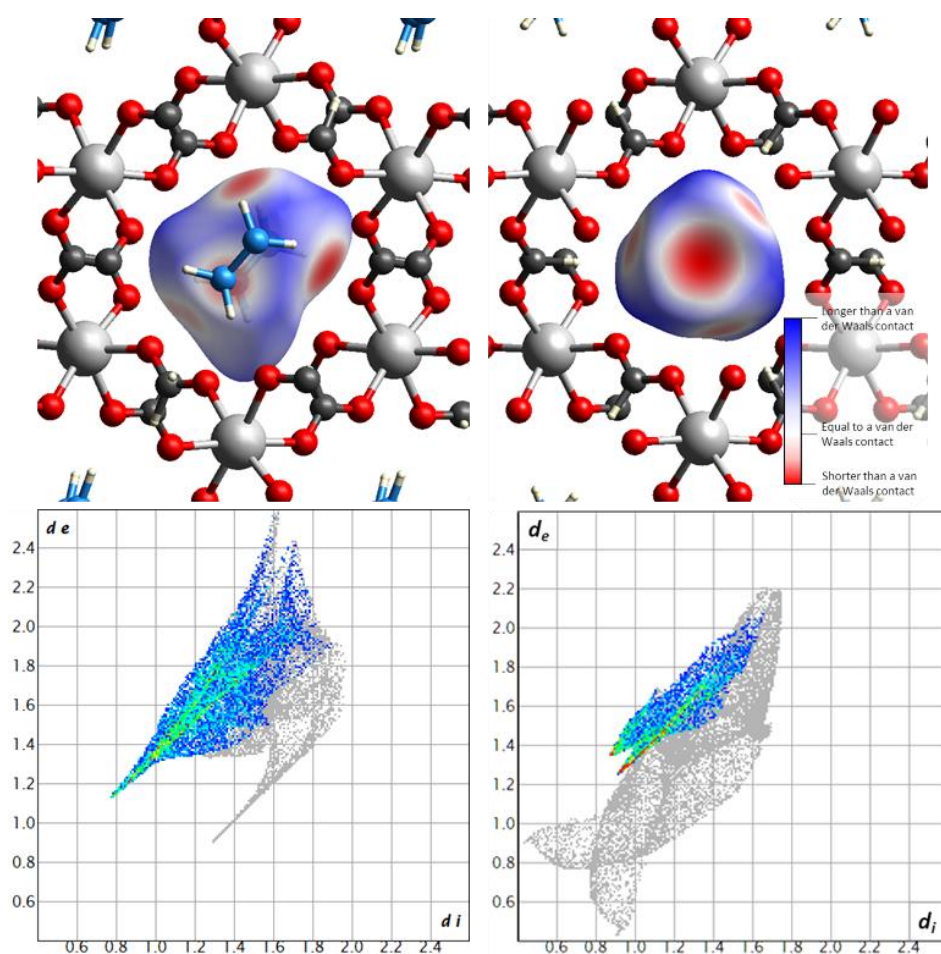
Fig. S2: Interatomic contacts between individual cation guests and the host framework displayed as a d_{norm} Hirshfeld surface and summarised as filtered fingerprint plots produced using the CrystalExplorer[1–3] software package showing H…O contacts for the $(NH_3NH_2)Mg(HCO_2)_3$ framework at (*left*) 250 K and (*right*) 400 K.

The Hirschfeld surface is computationally generated by calculating the molecular electron densities through stockholder portioning and illustrates the proximity of modelled atoms from within the surface (d_i), in this case the cation to all neighbouring external atomic sites (d_e), the framework.[3] From this the nature and comparative strength of intermolecular interactions between these atomic positions can be inferred.[2]

What can be clearly seen between the two phases is that there are strong interactions between the guest and host framework. At LT there is a distinct sharp feature that describes the interaction between the cationic guest and the framework as C=O…H-N interactions. The features in the HT plot is less diffuse with the frequency of interactions increased for shorter contacts shown by the red regions of the plot. The feature is also split showing a difference between the two crystallographically distinct NH_3 environments of the cation interacting with the framework. The HT plot is not a true reflection of all of the host guest contacts present in the HT due to the disorder of the cation preventing the modelling of all H positions for the guest residing perpendicular to the channel direction. As such this only gives information regarding the aligned cations and should be interpreted cautiously.
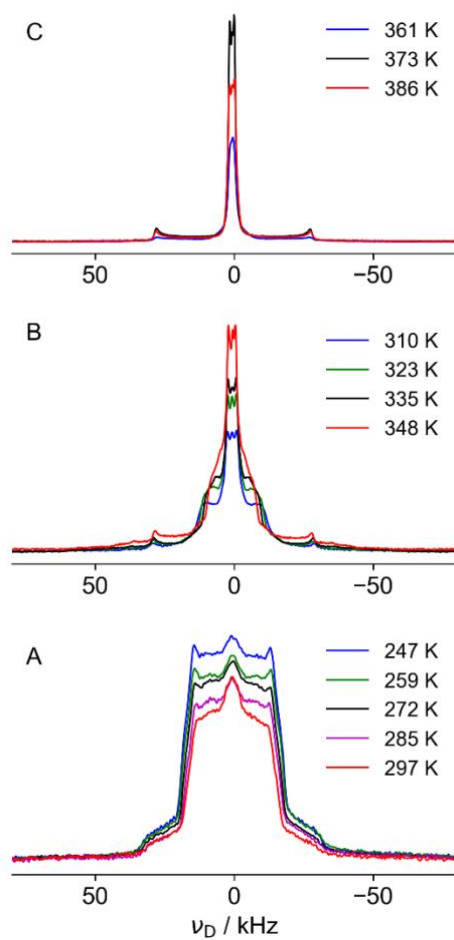
Solid-state NMR

Fig. S3: Overlaid ^{2}H NMR spectra for (A) low temperature structure, (B) intermediate regime and (C) high temperature structure. Where needed spectra have been scaled to an equivalent number of signal acquisitions to allow more meaningful comparison of spectral intensity.

Table S6: Fitting parameters[a] for the ^{2}H NMR spectra.

	259 K		335 K				386 K		
Fractional integral	0.68	0.32	0.17	0.58	0.23	0.01[b]	0.34	0.65	0.01[b]
δ_{iso} / ppm	6	7	4	10	9.4	8	3	9.1	9
C_Q / kHz	43	20	77	21	5.0	0	75	3.0	0
η	0.13	0.8	0.02	0.2	0.0	0	0.00	0.0	0
LB[c] / kHz	2	3	1.5	2.6	0.8	1.2	1.1	0.8	0.6

[a] Fitting values are shown to the number of significant figures required for a satisfactory visual fit of the data.
[b] Used to "fit out" a zero-frequency component; not physically significant.
[c] Lorentzian line-broadening.

The integral ratio of 0.68:0.32 differs measurably from the 3:2 ratio expected if the two sites correspond to ND$_3$ vs. ND$_2$. It is possible that a fraction of –ND$_2$ sites are dynamic within a symmetrical potential analogous to the potential experienced by the –ND$_3$ sites.

Relaxation fitting

The ^{1}H data relaxation is fitted using simple models based on isotropic rotational diffusion. Given the complexity of the system, more exact modelling is difficult, and would not, in any case, provide additional insight; the overall predicted curves for different motional models would be essentially indistinguishable, and, in particular, would give very similar values (within the fitting uncertainties) for the activation barrier E_a. It is also important to note that these models assume that all the ^{1}H spins are relaxing at the same rate, whereas the system is heterogeneous, both in terms of different H environments (hydrazinium vs. formate) and different cation populations, especially in the higher temperature regimes. Due to efficient ^{1}H "spin diffusion", the measured relaxation rate will be a weighted sum of the relaxation rates of the different H environments. Hence the fitted parameters and predicted rates from the mid and high temperature regimes should be treated as indicative of the dynamics rather than physically significant.

The T_1 data is fitted to:[4]

$$\frac{1}{T_1} = A[J(\nu_0) + 4J(2\nu_0)] \tag{1}$$

where A is a scaling / amplitude factor and $J(\nu)$, the spectral density, is defined as

$$J(\nu) = \frac{2\tau_c}{1 + (2\pi\nu\tau_c)^2} \tag{2}$$

where ν_0 is the NMR frequency of the nucleus involved and τ_c is the motional correlation time. Assuming a simple thermally activated motion, the temperature dependence of τ_c can be described using the Arrhenius equation to calculate the relaxation time constant as a function of temperature:

$$\tau_c = \tau_\infty \exp(E_a/kT) \tag{3}$$

The ^{1}H $T_{1\rho}$ data is fitted in a similar way except

$$\frac{1}{T_{1\rho}} = A_1 J_1(\nu_1) + A_2 J_2(\nu_1) \tag{4}$$

where the overall rate of relaxation is the sum of two components with distinct amplitude and thermal activation parameters, and the spectral density is sampled at ν_1, the nutation rate under RF irradiation (here 50 kHz) rather than the NMR frequency.

Table S7: Summary of NMR relaxation data fittings (data in Fig. 6).

Nucleus	Type	Temperature range / K	E_a / kJ mol^{-1}	$\log_{10}(\tau_0$ / s)	$\log_{10}(A$ / Hz)
^{1}H	T_1	222–314 (Low)	11.3(2)	−11.79(4)	9.248(2)
		361–384 (High)	6.58(12)	-	-
	$T_{1\rho}$	222–353 (Low)	13.3(8)	−8.57(16)	7.923(8)
			49(7)	−13.2(12)	7.55(5)
^{2}H	T_1	247 − 286 (Low)	9.4(4)	-	-
		348 − 386 (High)	13.0(9)	-	-

The apparent activation energy of 11.3 kJ mol^{-1} from the ^{1}H T_1 data in the low temperature region should be interpreted cautiously, since the broad minimum of Fig. 6 will be a superposition of curves from both NH$_3$ and NH$_2$ sites. It is interesting to contrast to the material Li(N$_2$H$_5$)SO$_4$,[5] in which the NH$_3$ and NH$_2$ dynamics are resolved in ^{1}H $T1$ relaxation measurements, due to major differences in hydrogen bonding. In the latter material, and contrasting to the MOF material under study, the ND$_3$ group is not significantly hydrogen bonded, and so has measurably faster rotation rate (the relaxation minimum is at 190 K for a ^{2}H frequency of 27 MHz), but a larger activation barrier of 18 kJ mol^{-1} (4.3 kcal mol^{-1}). This suggests that the values obtained here are of limited physical significance. The $T_{1\rho}$ minimum in the low temperature phase is also likely to reflect the ND$_n$ motion, but the fitting is much less robust as the minimum is poorly defined. Indeed, the predicted motional rates from the fitted $T_{1\rho}$ parameters are significantly smaller than those from T_1 (the τ_0 parameter is over three orders of magnitude larger). This is consistent with the fitting being over-simplified.
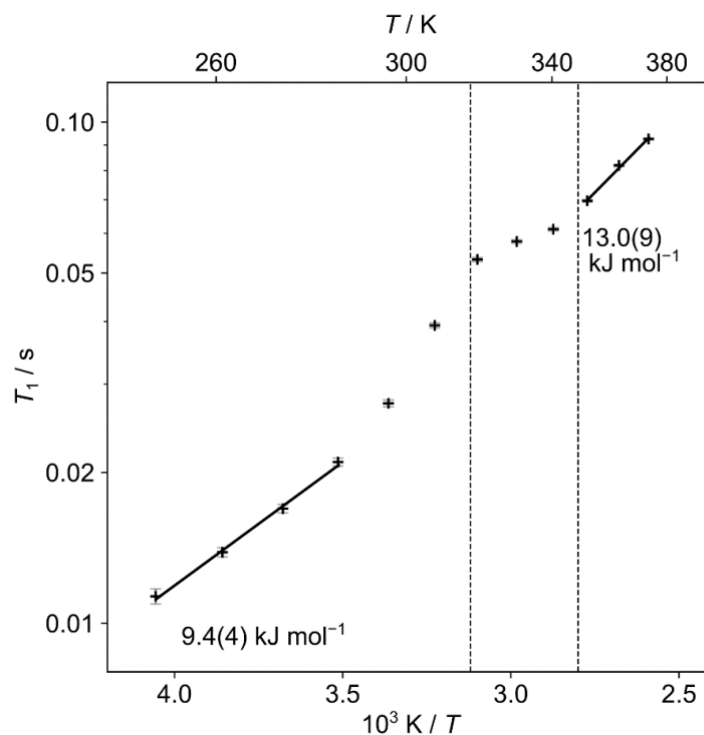
Fig. S4: ^{2}H T_1 relaxation time constants as a function of temperature for static samples of (ND$_3$ND$_2$)Mg(HCO$_2$)$_3$ at 76.7 MHz. The data was acquired using saturation recovery experiments and analysed in the same way as the ^{1}H data. The lower temperature data showed some deviations from single exponential behaviour, but a simple single-exponential fit was used to capture the temperature dependence, and show that this is consistent with the more extensive ^{1}H relaxation data.
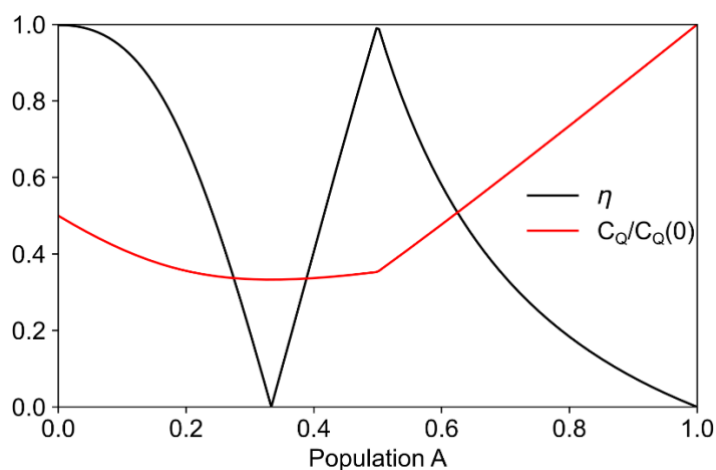

Fig. S5: Dependence of the averaged quadrupolar coupling tensor in the limit of fast exchange between three sites as a function of the population of site A, with B and C equally sharing the remaining population. This mimics the exchange of ND$_2$ about the N–N bond in a potentially non-symmetric potential. The cone angle is 70.5°. $A = 1/3$ corresponds to the normal case of symmetric three-site exchange, resulting in an asymmetry η of 0, and a strong scaling of the quadrupole coupling, C_Q (scaling of 0.33). Even small changes in site occupancies lead to significant deviation from $\eta = 0$. Data calculated using NMR Weblab.[6]
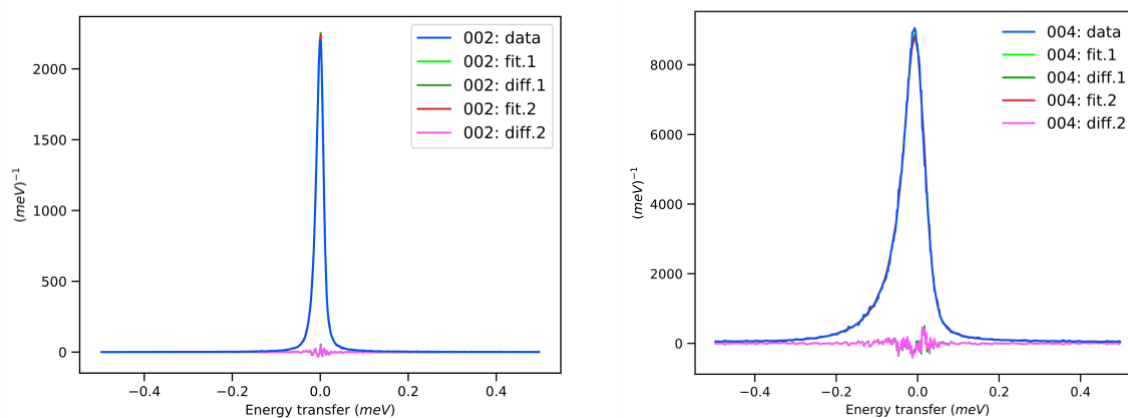
9

QENS

Fig. S6: Representative fits to two Lorentzian overlaid with the difference curve showing little difference between the two fits, for (left) PG(002) configuration and (right) the PG(004) configuration.
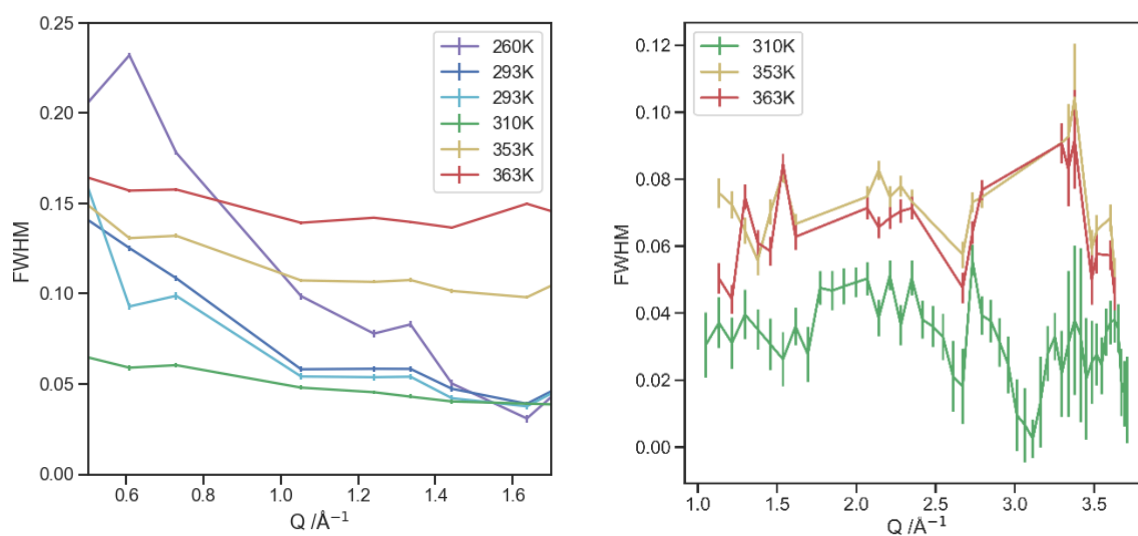

Fig. S7: FWHM of the quasielastic peak for (left) in the PG(002) configuration and (right) in the PG(004) configuration

At temperatures below 300 K, there is significant peak broadening at lower Q, which is then suppressed at higher temperatures. This is likely a multiple scattering artefact due to the low amplitude of the Lorentzians at lower Q for lower temperatures and is unlikely to be physically meaningful.

LT EISF Model

To model the low temperature QENS data we used the standard expressions for the EISF with the spherical (zero order) Bessel function, j_0, to describe the combination of jumps between three equivalent sites on a circle of radius, r, and jumps between two equivalent sites across a distance, d.[7] These are used to describe the NH_3 groups and NH_2 groups respectively, modelling the molecular picture revealed by NMR without considering the disorder of the crystallographic model. The EISF expression for each molecular components that contribute to the observed motion are combined and weighted to reflect the stoichiometric ratio of hydrogens per cation. We refined a linear transformation (6), along with variables, f, the fraction of molecules contributing to the motion on the IRIS timescale and, m, multiple scattering effects correction to prevent the EISF tending to 1 as Q becomes 0.[7]

$$A_0(Q) = \frac{1}{3}\left[1 + 2j_0(Qr\sqrt{3})\right] \tag{5}$$

$$B_0(Q) = \frac{1}{2}\left[1 + j_0(Qd)\right] \tag{6}$$

$$A^{A_0 B_0}(Q) = (1 - f) + fm \frac{1}{5}\left[3A_0 + 2B_0\right] \tag{7}$$

HT EISF Model

The high temperature QENS data was more complex due to the additional 7th hydrogen site that sits between the reorientated cations. Following on directly from equation (2.220b) in Ref 7, the standard expressions for the EISF with the spherical (zero order) Bessel function, j_0, was used to describe all possible exchanges between the sites, r_{ik}, where are i and k are observable hydrogen sites, see Table S8. The occupancy of the exchanging sites is also considered by the fractional occupancy variables, f_i, and f_k. These r_{ik}, f_i, and f_k parameters are explicitly calculated from the neutron crystallography and not refined, with values below in Table S9. For simplicity and to avoid over parameterisation the seven sites were classified as six exterior and one interior, with the occupancy of the interior site set as 0.4 consistent with the neutron crystallography and the exterior to 0.767, calculated as the mean occupancy of the exterior sites. These were again combined with multiple scattering correction, m, and the fraction of molecules contributing to the motion on the IRIS timescale, f, presented in Table S10.[7]

$$A_0(Q) = \left(\sum_i f_i\right)^{-2} \left[\sum_i f_i^2 + 2\sum_{i<k} f_i f_k j_0(Qr_{ik})\right] \tag{8}$$

$$A^{A_0}(Q) = (1-f) + fm[A_0] \tag{9}$$

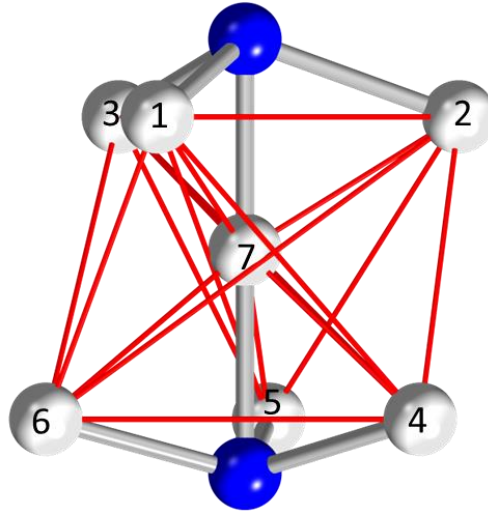The fits to the experimental QENS data are shown in Fig. 7 of the main text and Fig. S9 below.

Fig. S8: Visualisation of the r_{ik} site jumps showing how these relate to two adjacent cations.

Table S8: Site exchanges, r_{ik}, where $i<k$.

i	k	i	k	i	k	i	k	i	k	i	k
1	2	1	3	1	4	1	5	1	6	1	7
2	3	2	4	2	5	2	6	2	7	2	
3	4	3	5	3	6	3	7	3		3	
4	5	4	6	4	7	4		4		4	
5	6	5	7	5		5		5		5	
6	7	6		6		6		6		6	
7		7		7		7		7		7	

The high symmetry of the system equivalates some of these exchanges, reducing them to seven unique site exchanges, shown in Table S9

.

Table S9: Values for the distances of the r_{ik} site exchanges used in HT model and determined from the neutron crystallography.

Symmetry equivalent r_{ik}	Distance/ Å
r_{12}, r_{13}, r_{23}	2.050
r_{45}, r_{46}, r_{56}	2.030
r_{14}, r_{25}, r_{36}	1.854
r_{15}, r_{26}, r_{34}	2.214
r_{16}, r_{24}, r_{35}	2.852
r_{17}, r_{27}, r_{37}	1.378
r_{47}, r_{57}, r_{67}	1.501

Table S10: Refined values for the fraction of cations contributing to the motion on the IRIS timescale, f and m.

Temperature/ K	f	m
260	0.13(2)	0.77(3)
293	0.29(2)	0.87(2)
293	0.35(2)	0.87(3)
310	0.44(3)	0.86(4)
353	0.48(1)	0.81(2)
363	0.63(2)	0.82(4)

A single Lorentzian component was fitted to the quasielastic peak:

$$L(x) = \frac{\hbar}{\pi} \frac{\frac{1}{2}\Gamma}{(x - x_0)^2 + \left(\frac{1}{2}\Gamma\right)^2} \tag{10}$$

The mean residence times τ for the hydrogen atoms at each site were calculated from the mean FWHM Γ by comparing the general functional form to the corresponding part of the $S(Q, \omega)$ function for the relevant model: [7]

$$\frac{1}{\pi} \frac{2\tau}{4 + \omega^2\tau^2} \text{ (Low T)} \tag{11}$$

$$\frac{1}{\pi} \frac{3\tau}{9 + \omega^2\tau^2} \text{ (High T)} \tag{12}$$

This simplifies to

$$\Gamma = \frac{2\lambda}{\tau} \tag{13}$$

where $\lambda = 2$ at low temperature and $\lambda = 3$ at high temperature. Full $S(Q, \omega)$ can be found in reference 7 as equations (6.42) and (6.51), respectively.
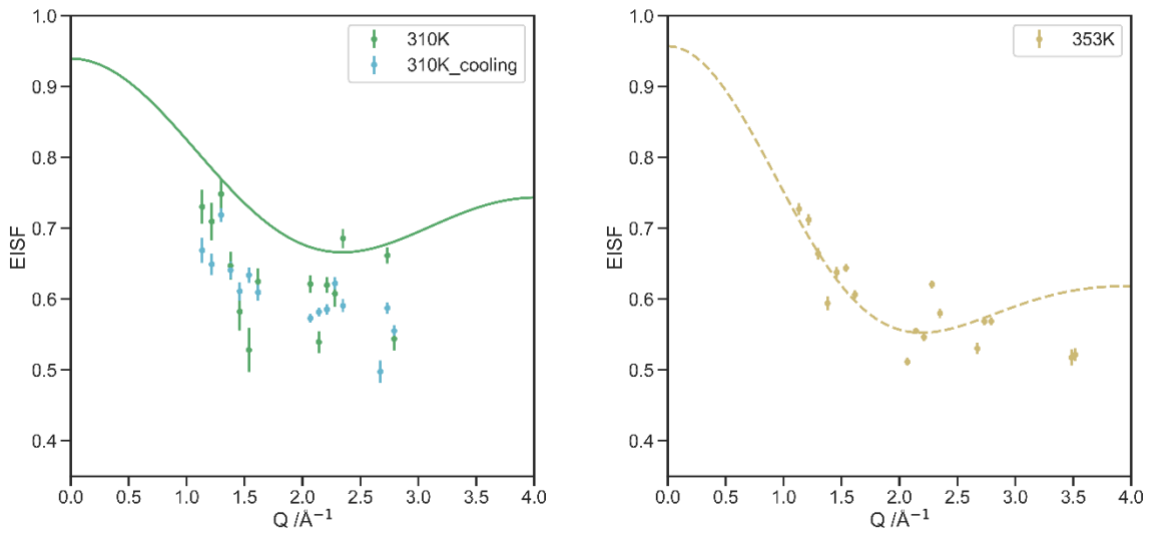
Fig. S9: EISF for the data collected in the PG(004) configuration with the overlaid model that was fitted to the PG(002) data for (left) 310 K data sets and (right) the 353 K dataset.

Fig. S9 show the comparison of the model fitted to the PG(002) configuration to the QENS data collected in the PG(004) configuration. This setup provides a larger Q-range at the trade-off of resolution. A comparison of how the models match the PG(004) data is below in Fig. S10. Along with the models plotted without any of the refined parameters or experimental data, highlighting the difference between the low temperature and high temperature models.
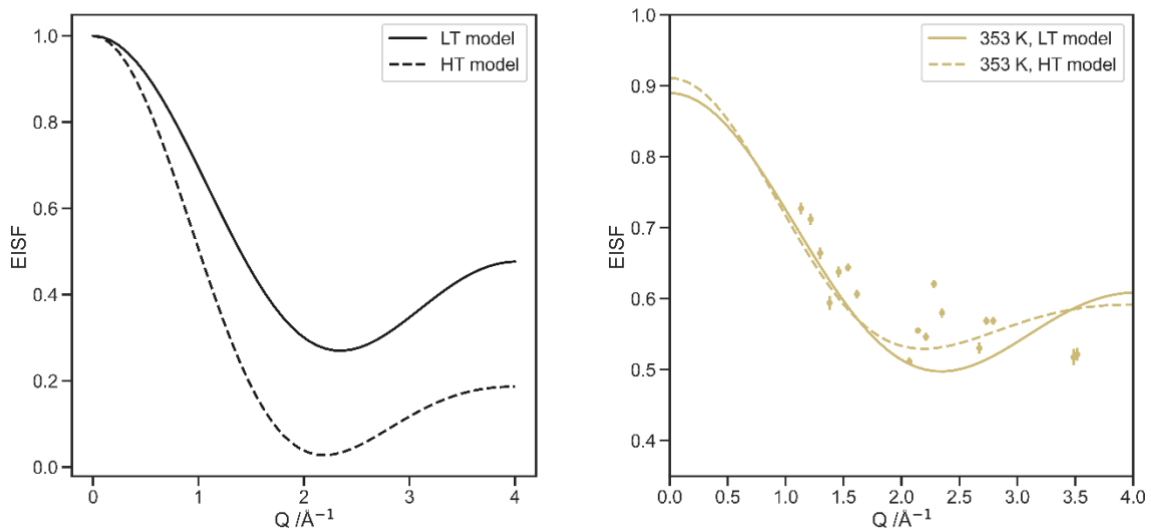
Fig. S10: (left) EISF models plotted without fitting to experimental data and with refinable parameters f and m removed to show the difference in the models. (right) The EISF models, with refinable parameters f and m, fit to the PG(004) data collected at 353 K.

Dielectric Behaviour

The Arrhenius law can be used to interpret the dielectric data measured at low frequency:

$$f = f_0\, exp(-E_a/RT) \qquad\qquad (14)$$

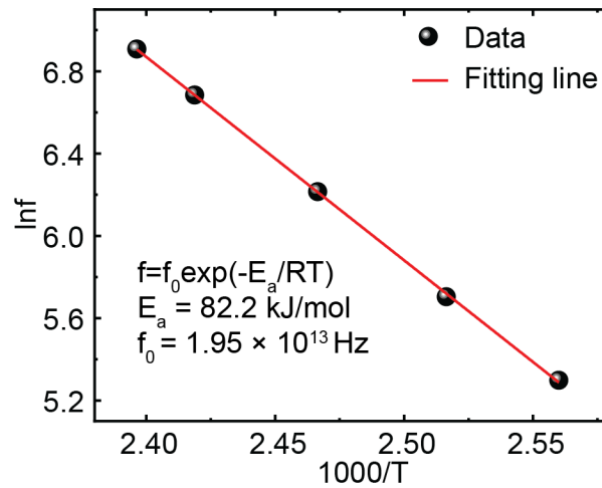where the E_a is the activation energy, f_0 is the relaxation frequency constant, and T is the peak temperature of tanδ.

Fig. S11: The plot between ln(f) and 1000/T, where T is peak temperature of tanδ, according to the Arrhenius law

Powder X-Ray Diffraction
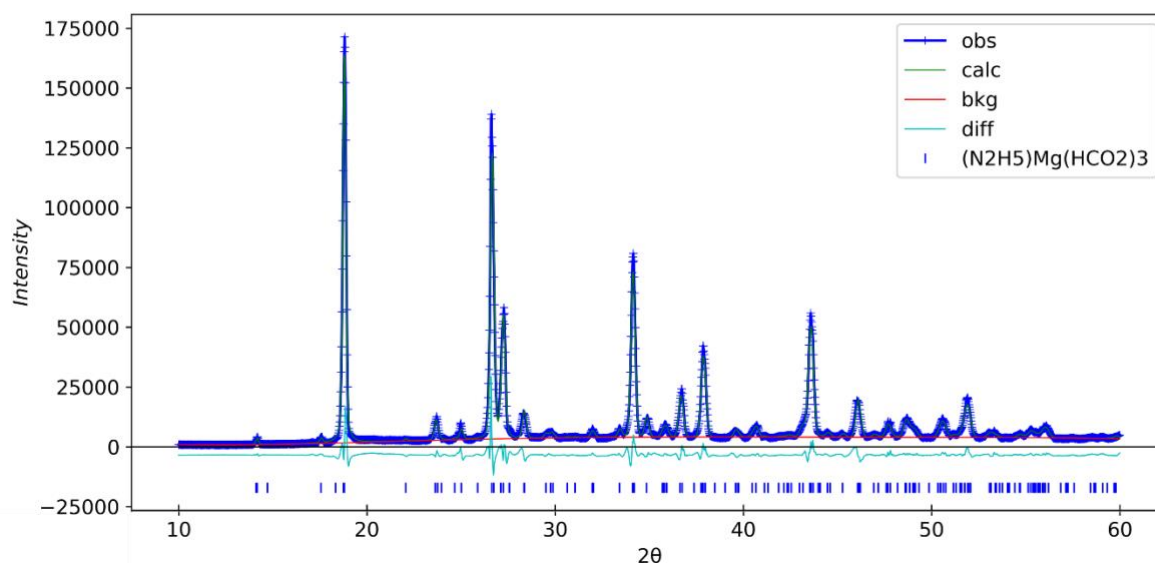

Fig. S12: Le Bail fit showing the phase purity for the selectively deuterated sample used for QENS analyses where a = 7.4874(8) Å, b = 7.8896(7) Å, c = 13.7075(14) Å and V = 809.74(10) Å^3. Rp = 7.30 %, wR = 10.46 %, and reduced χ^2 = 26.98.

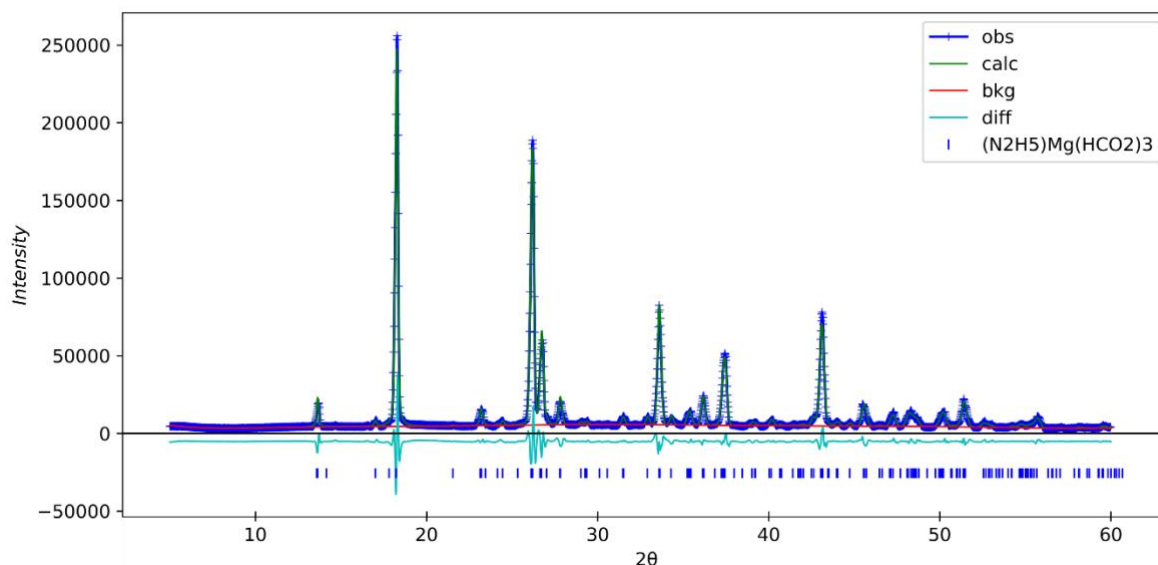Fig. S13: Le Bail fit showing the phase purity for the deuterated sample used for SSNMR analyses where a = 7.5095(6) Å, b = 7.9238(8) Å, c = 13.8160(8) Å and V = 822.11(13) Å^3. Rp = 7.58 %, wR = 10.13 %, and reduced χ^2 = 18.44.

References

1   P. R. Spackman, M. J. Turner, J. J. McKinnon, S. K. Wolff, D. J. Grimwood, D. Jayatilaka and M. A. Spackman, *J. Appl. Crystallogr.*, 2021, **54**, 1006–1011.

2   M. A. Spackman and J. J. McKinnon, *CrystEngComm*, 2002, **4**, 378–392.

3   M. A. Spackman and D. Jayatilaka, *CrystEngComm*, 2009, **11**, 19–32.

4   D. C. Apperley, R. K. Harris and P. Hodgkinson, *Solid-State NMR: Basic Principles and Practice*, Momentum Press, New York, 2012.

5   R. R. Knispel and H. E. Petch, *Can. J. Phys.*, 2011, **49**, 870–875.

6   V. Macho, L. Brombacher and H. W. Spiess, *Appl. Magn. Reson. 2001 203*, 2001, **20**, 405–432.

7   M. Bée, *Quasielastic neutron scattering: Principles and applications in solid state chemistry, biology and materials science*, Adam Hilger, IOP Publishing, Bristol and Philadelphia, 1989.